AGU PUBLICATIONS

JGR

Journal of Geophysical Research: Oceans

RESEARCH ARTICLE

10.1002/2013JC009591

Special Section:
Western Pacific Ocean Circulation and Climate

Extending our understanding of South Pacific gyre "spin-up": Modeling the East Australian Current in a future climate

E. C. J. Oliver[1,2] and N. J. Holbrook[1,2]

[1]Institute for Marine and Antarctic Studies, University of Tasmania, Hobart, Tasmania, Australia, [2]Australian Research Council Centre of Excellence for Climate System Science, Hobart, Tasmania, Australia

Key Points:
- EAC extension transport is projected to increase
- Transport along Tasman Front is projected to decrease
- Changes consistent with linear barotropic model and basin-wide wind stress curl

Correspondence to:
E. C. J. Oliver,
eric.oliver@utas.edu.au

Citation:
Oliver, E. C. J., and N. J. Holbrook (2014), Extending our understanding of South Pacific gyre "spin-up": Modeling the East Australian Current in a future climate, *J. Geophys. Res. Oceans*, *119*, 2788–2805, doi:10.1002/2013JC009591.

Received 9 NOV 2013
Accepted 21 APR 2014
Accepted article online 23 APR 2014
Published online 12 MAY 2014

Abstract The western Tasman Sea represents a global warming marine "hot spot," where the waters are warming at almost 4 times the global average rate, argued in the literature to be due to a "spin-up" of the South Pacific subtropical gyre and extension of the East Australian Current (EAC). To further investigate and test this paradigm, we analyze climate change simulations of Tasman Sea circulation and metrics on output from the Ocean Forecasting Australia Model for the 20th and 21st centuries, forced by a global climate model simulation under the A1B carbon emissions scenario. First, we show that the 1990s simulation estimates of mean dynamic topography, present-day location of the EAC separation point, and volume transports of the EAC, EAC extension, and flow along the Tasman Front, are consistent with recent observations. We further demonstrate that between the 1990s and 2060s, the volume transport of the EAC extension is projected to increase by 4.3 Sv at the expense of the flow along the Tasman Front (projected to decrease by 2.7 Sv). The transport of the EAC core flow (equatorward of the separation point) is projected to change very little (increase of 0.2 Sv). The model projects a Tasman Sea-wide warming, with mean increases of up to 3°C. These results are interpreted using a simple linear, barotropic model which captures both the sign and meridional distribution of the projected changes in mean transport, including negligible change in core EAC transport but enhanced EAC extension. This meridional asymmetry in the transports is consistent with the wind-forced ocean response to changes in the basin-wide wind stress curl.

1. Introduction

The subtropical western boundary current regions are hot spots for global climate change [*Wu et al*., 2012]. In the South Pacific Ocean, the surface and near surface waters of the southwest Tasman Sea, focused between Tasmania and ~150°E, have been warming at ~3–4 times the global average rate for the past few decades [*Holbrook and Bindoff*, 1997; *Ridgway*, 2007]. This warming is having significant impacts on the marine ecology off southeastern Australia, with warm-water species moving poleward and displacing the indigenous cold-water species, and where any further migration or displacement of coastal species is limited by the southward extent of the continental shelf just south of Tasmania [*Last et al*., 2010; *Johnson et al*., 2011]. Accurate projections of ocean climate change for this region, and a better understanding of the underlying physical mechanisms governing these changes, are important in order to appropriately inform the development of adaptation strategies for marine species.

The western boundary current of the South Pacific, consisting of the southward flowing East Australian Current (EAC) and EAC extension, as well as the eastward flow along the Tasman Front and complex currents around New Zealand, appears to have undergone significant changes in recent years. *Roemmich et al*. [2007] estimate that the South Pacific subtropical gyre sea surface height pattern increased by 12 cm between 1993 and 2004 with the maximum change occurring just east of New Zealand—and refer to this as a "spin-up of the gyre." These changes are identified as a gyre-scale response to an increase in the wind stress curl east of New Zealand. Parallel research suggests that the observed multidecadal increases in temperature and salinity recorded at Maria Island off Tasmania's east coast are due to a southward penetration (extension) of the EAC between 1945 and 2007 [*Ridgway*, 2007]. *Hill et al*. [2008] further suggest that the observed interannual to decadal scale changes in temperature and salinity at Maria Island are due to basin-scale wind forcing changes in the South Pacific, with the 3 year lag response being too short for the influence of remote baroclinic Rossby waves. Using ocean state estimates from reanalysis data, *Hill et al*. [2011] further show that a 3 year lag correlation is also apparent between the southward transport in the EAC and

decadal variations in the basin-wide South Pacific wind stress curl, at the expense of eastward flow along the Tasman Front to New Zealand. This 3 year lag is also identified in a linear, reduced-gravity ocean modeling study by *Holbrook et al*. [2011] to be consistent with decadal El Niño-Southern Oscillation (ENSO) scale forcing across the South Pacific that connects the EAC upper ocean transports with observed sea levels in Sydney, with baroclinic Rossby waves being the important explanatory mechanism for these changes. In the mean, *Cai et al*. [2005] and *Cai* [2006] show that high-latitude changes in wind stress curl can lead to changes not only in the circulation of the South Pacific Gyre but also in the circulation of the southern hemisphere "supergyre" which links the three southern hemisphere subtropical gyres.

In this study, we have used dynamically downscaled global climate change projections to examine changes in the marine climate of the Tasman Sea region, with particular focus on the western boundary current system. We build upon the studies by *Chamberlain et al*. [2012] and *Sun et al*. [2012], which detail the dynamically downscaled global climate projections and the impact of climate change on the large-scale circulation around Australia. The present study also builds upon the research by *Matear et al*. [2013], which examines the climate change signal in the Tasman Sea with a particular focus on the change in eddy activity and associated increase in nutrient supply and primary productivity in the upper ocean, and upon *Oliver et al*. [2014], which focused on the projected changes in Tasman Sea surface temperature extremes. Here we focus on changes in the mean circulation, and demonstrate that the core EAC transport into the Tasman Sea is projected to change very little, while the poleward transport by the EAC extension is increased at the expense of the eastward transport along the Tasman Front. We apply a linear barotropic model based on the Sverdrup transport and *Godfrey* [1989] Island Rule to show that the transport changes in the western boundary current are consistent with changes in basin-wide South Pacific wind stress curl, in terms of both the sign and meridional distribution.

This paper is outlined as follows: the dynamically downscaled ocean model and observations used for validation are presented in section 2. In section 3, we present an overview of the general bathymetry and circulation in and around the Tasman Sea. In section 4, we compare the ocean model projections of the mean circulation pathways and transports through the Tasman Sea. In section 5, we estimate the position of the EAC separation point for the 1990s against observations and provide estimates of the model projected changes between the 1990s and 2060s. The relative changes in volume transport of the EAC, EAC extension, and flow along the Tasman Front are interpreted in section 6 using the simple linear barotropic model forced by surface wind stress fields for the 1990s and the 2060s. A summary and discussion is presented in section 7.

2. Data

We used dynamically downscaled ocean model simulations for the 1990s and 2060s decades to investigate the ocean circulation response to climate change in the Tasman Sea. The downscaling was performed using the Ocean Forecasting Australia Model (OFAM) [*Oke et al*., 2008] forced by a reanalysis representation of the present-day climate and by a global climate model projection of climate change (using the CSIRO Mk3.5 climate model under an A1B emissions scenario) [*Chamberlain et al*., 2012; *Sun et al*., 2012]. OFAM runs quasi-globally (70°S and 70°N) with 47 *z*-levels in the vertical (with 10 m resolution in the upper 200 m) and 1/10° horizontal resolution (eddy-resolving) in the greater Australia region (90°E to 180°E, 70°S to 20°N) coarsening outside of this domain gradually up to 2° horizontal resolution in the North Atlantic Ocean.

The model forcing fields were developed as follows [*Chamberlain et al*., 2012; *Sun et al*., 2012]. In the control (CTRL) simulation, OFAM was forced repeatedly by "normal year" forcing representing the decade of the 1990s. This "normal year" forcing comprises ocean surface fluxes of heat, freshwater, and momentum generated from European Centre for Medium-Range Weather Forecasts (ECMWF) Reanalysis output (ERA-40) [*Uppala et al*., 2005] and filtered so that variability on time scales of 1 year or less are retained but major climate variability modes such as El Niño, Indian Ocean Dipole, etc., are in neutral states (see *Chamberlain et al*. [2012], for details on the ocean model and forcing fields). Therefore, the forcing fields contain no variability on interannual (or longer) time scales. Global climate model (CSIRO Mk3.5) simulations, forced under the A1B emissions scenario, provide climate change projections through the 21st century. In what we refer to as the A1B simulation, OFAM was forced by modified fields generated by adding the CSIRO Mk3.5 projected change between the 1990s and 2060s decades to the normal year forcing. We obtained mean fields

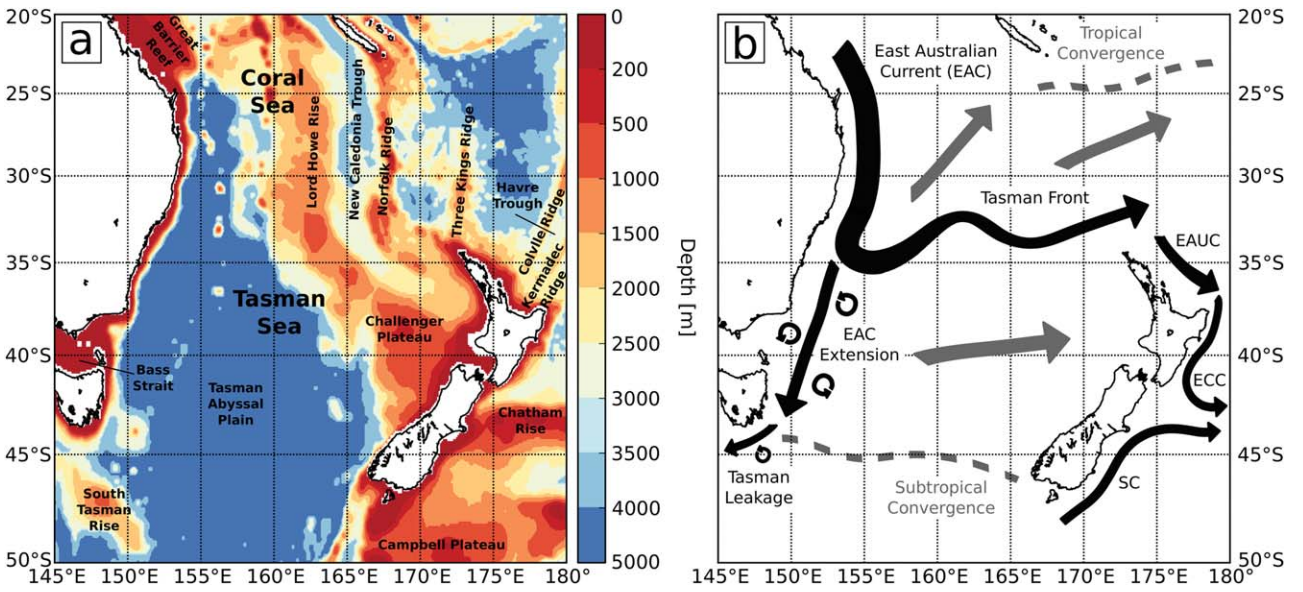

Figure 1. Tasman Sea bathymetry and general circulation. (a) Colors indicate the bathymetric depths across the region, from OFAM, with notable seas and bathymetric features identified. (b) Schematic of the regional oceanography including ocean currents and fronts. EAUC = East Auckland Current, ECC = East Cape Current, SC = Southland Current.

of sea surface height (SSH) and three-dimensional circulation from the last 9 years of the CTRL and A1B simulations over the domain bounded by 140°E, 180°E, 50°S, and 20°S.

We obtained two estimates of mean dynamic topography (MDT) based on oceanographic observations. The MDT relative to 2000 m was obtained from the CSIRO Atlas of Regional Seas (CARS) climatology (www.cmar.csiro.au/cars) [*Ridgway et al*., 2002; *Dunn and Ridgway*, 2002; *Condie and Dunn*, 2006], which has been mapped using a loess filter approach from historical temperature and salinity in situ observations. We also obtained the CNES/CLS 2009 MDT from Archiving, Validation, and Interpretation of Satellite Oceanographic Data (Aviso, http://www.aviso.oceanobs.com), which is a multivariate combination of MDT estimates remotely sensed from the Gravity Recovery and Climate Experiment (GRACE) and from in situ Argo and conductivity-temperature-depth (CTD) measurements [*Rio et al*., 2011].

3. The Bathymetry and General Circulation of the Tasman Sea

The bathymetry of the southwest Pacific is complex (Figure 1a). The western boundary (146°E–154°E) is formed primarily by the Australian continent which has a very narrow continental shelf, except in the region of the Great Barrier Reef (equatorward of 25°S). The Tasman Sea, containing the broad and deep Tasman Abyssal plain (>4000 m depth), extends between Australia and New Zealand approximately from 30°S to 50°S. A series of meridionally oriented ridges and troughs are found east and northeast of the Tasman Sea between 160°E and 180°E: Lord Howe Rise, New Caledonia Trough, Norfolk Ridge, Three Kings Ridge, Colville Ridge, Havre Trough, and Kermadec Ridge. These ridges and troughs extend into the Coral Sea and lead into the archipelagos of New Caledonia, Vanuatu, and Fiji, each with their own complex bathymetries. At the southern end of these ridges and troughs lies New Zealand, and the Challenger Plateau to its west makes the eastern Tasman Sea relatively shallow. To the southeast of New Zealand lies the shallow Chatham Rise and Campbell Plateau regions and to the south of Tasmania lies the South Tasman Rise.

The general ocean circulation in and around the Tasman Sea is shown schematically in Figure 1b. The South Equatorial Current, which flows westward between 10°S and 20°S (not shown), forms the northern boundary of the South Pacific subtropical gyre. Upon reaching the western boundary at ~18°S, it bifurcates [*Scully-Power*, 1973; *Church*, 1987] leading to northward flow, the Hiri Current, as part of the Coral Sea Gyre and southward flow as the western boundary current of the South Pacific Subtropical Gyre (not shown). The southward flow intensifies as the EAC [*Godfrey et al*., 1980], the primary western boundary current in the South Pacific, which has intense southward flow (25–37 Sv) [*Ridgway and Dunn*, 2003] between 27°S and

33°S. Between 32°S and 35°S, the EAC separates from the coast [e.g., *Godfrey et al*., 1980; *Ridgway and Dunn*, 2003] and undergoes a retroflection before forming a broad meandering eastward outflow approximately along the Tasman Front in the northern Tasman Sea [*Denham and Crook*, 1976; *Stanton*, 1979; *Boland and Church*, 1981]. Part of the flow along the Tasman Front continues eastward into the open Pacific Ocean and part of it reattaches to the western boundary along the northern coast of New Zealand, forming the East Auckland Current (EAUC) and East Cape Current (ECC), before separating again at about 42°S [*Heath*, 1985; *Stanton et al*., 1997; *Tilburg et al*., 2001]. The separation of the EAC that occurs at 32–35°S off eastern Australia is in fact only a partial separation, albeit the largest part. The remaining reduced flow—referred to as the EAC Extension—is eddy-rich and highly variable and continues southward along Australia's eastern shelf break to Tasmania [*Ridgway and Dunn*, 2003; *Suthers et al*., 2011; *Brassington et al*., 2011]. A small portion of this flow continues westward around the southern tip of Tasmania, forming what is called the Tasman Leakage [*Speich et al*., 2002] or Tasman Outflow [*Ridgway and Dunn*, 2007], and which links the Pacific Ocean and Indian Ocean subtropical gyre circulations. The remainder is dissipated as it leaves the shelf and interacts with the strong Antarctic Circumpolar Current or joins the general eastward drift across the Tasman Sea toward New Zealand [*Tilburg et al*., 2001; *Ridgway and Dunn*, 2003].

4. Validation of OFAM Mean Circulation

In this section, we evaluate the ocean model representation (simulation for the 1990s) of mean dynamic topography (section 4.1), geostrophic and Ekman volume transports (sections 4.2 and 4.3), the location of the EAC separation point (section 4.4), and the eddy kinetic energy (section 4.5) against observed estimates.

4.1. Surface Mean Dynamic Topography

The mean dynamic topography (MDT) of the ocean surface defines the surface currents, and these are indicative of the mass transports through the region—hence, MDT can be used to describe the general pattern of geostrophic flow [e.g., *Gill*, 1982]. The ocean model captures well the observed general structure of the MDT in the Tasman Sea (Figure 2). The EAC is evident in both the CTRL simulation and the observations as a strong zonal gradient in MDT across the continental shelf of eastern Australia between about 23°S and 34°S at which point there is a partial separation of flow from the continental shelf. In both the model and observed fields, the majority of the southward flow separates from the shelf in the vicinity of 33–34°S and retroflects with some of the flow being recirculated through a quasi-standing anticyclonic eddy, and forms a broad eastward flow across the northern edge of the Tasman Sea (the Tasman Front). The recirculation is much stronger in the model than in the observations; also, the Tasman Front is narrower and oriented more zonally in the model than in the observations where it has a small northward component. The observed general eastward flow to the north of New Zealand and partial reattachment to the western boundary along the northern and eastern coasts of New Zealand followed by a second separation around 42°S–43°S is evident in the model fields, although the model seems to predict a larger degree of reattachment along northern New Zealand and a weaker boundary current south of East Cape than is observed. Finally, the model captures the EAC extension flow, that portion of the EAC that does not separate from the shelf, along the coast of Australia poleward of ∼33°S including its weakening at higher latitudes as the flow continually leaves the shelf and forms a general eastward drift across the Tasman Sea. It should be noted that the model simulated EAC extension flow through the Tasman Sea tends to be narrower than the observed estimates. Nevertheless, as will be shown in section 4.3, the model estimates of these volume transports are consistent with observations.

4.2. Geostrophic and Ekman Depth-Integrated Currents

The depth-integrated geostrophic flows (U_g, V_g) (Figure 3a) were estimated from the depth-integrated steric height relative to 2000 dbar (h_{2000}; Figure 3b), following *Ridgway and Godfrey* [1994] (henceforth RG94) and *Ridgway and Dunn* [2003], and compared with those simulated by the ocean model (Figures 3c and 3d). From the CARS temperature and salinity climatology, the full vertical structure of steric heights relative to 2000 dbar was calculated (i.e., steric heights as function of depth through the water column) and integrated from the surface to 2000 dbar to yield h_{2000}. The reference level of 2000 dbar (level of no motion) was chosen to be consistent with previous studies (RG94) [*Ridgway and Dunn*, 2003]. In regions, where the bathymetry occupies depths shallower than 2000 m, we linearly interpolated h_{2000} in (x, y) space across this

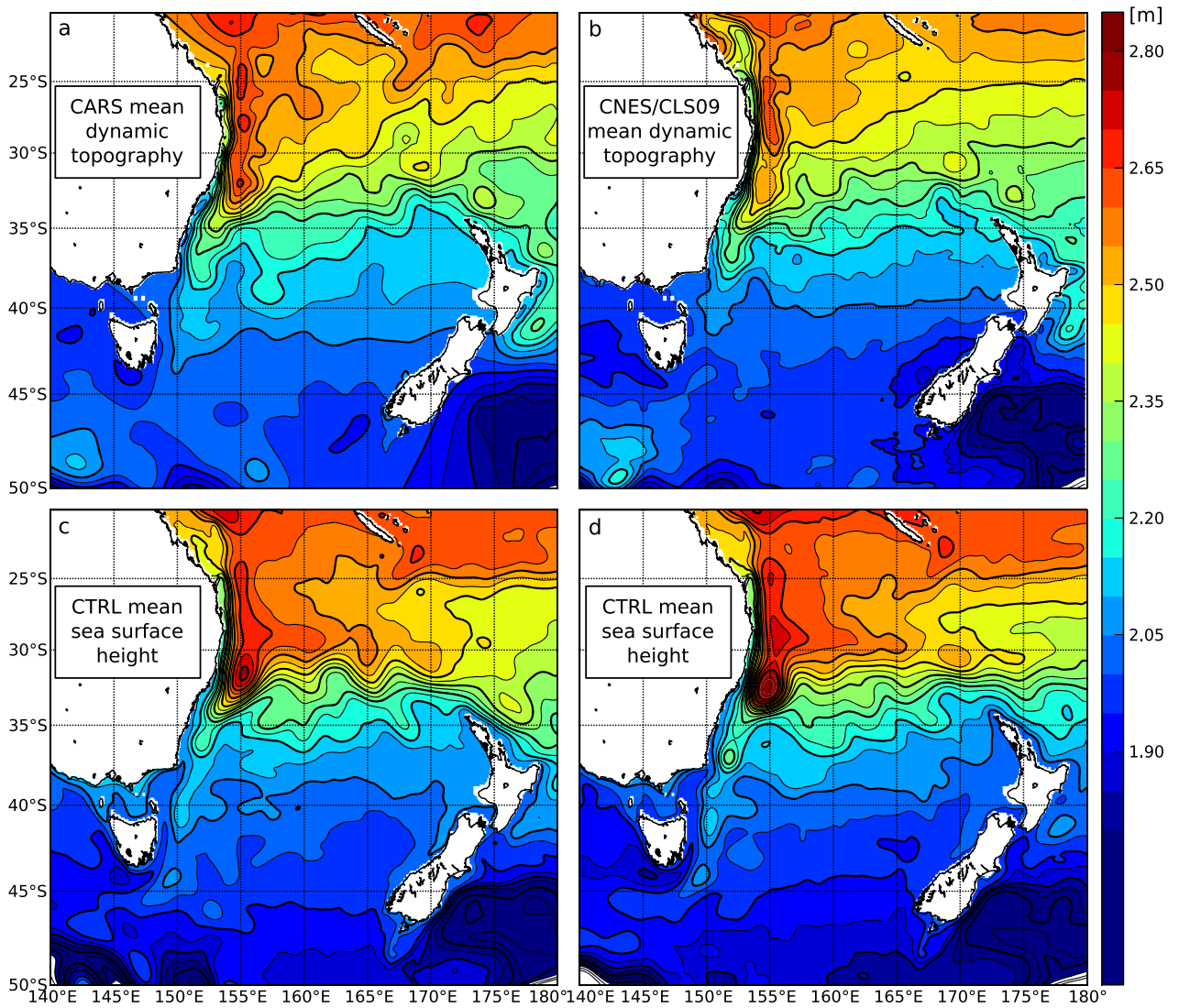

Figure 2. Mean dynamic topography (MDT) of the Tasman Sea surface. MDT is shown (a) estimated from CARS temperature and salinity fields to a reference depth of 2000 m, (b) derived from remotely sensed and in situ observations by Aviso (CNES/CLS09 MDT), and from the (c) CTRL and (d) A1B ocean model simulations. Note that mean sea surface height is equivalent to the MDT for the ocean models since there is no model geoid. The datum level of MDT from CNES/CLS09 and the ocean model simulations have been offset so that they have the same value as the CARS MDT at the reference location (165°E, 35°S).

bathymetry. The depth-integrated geostrophic currents were estimated by calculating the horizontal gradient of h_{2000} [e.g., *Godfrey*, 1989; *IOC et al.*, 2010] according to

$$(U_g, V_g) = \frac{g}{f}\left(-\frac{\partial h_{2000}}{\partial y}, \frac{\partial h_{2000}}{\partial x}\right), \tag{1}$$

where $g = 9.8$ m s^{-2} is the gravitational acceleration and f is the Coriolis parameter (Figure 3a). For the ocean model simulation, we first calculated the steady state depth-integrated Ekman transport (U_E, V_E) using the wind stress forcing fields τ [e.g., *Gill*, 1982, equation (9.2.7)] and

$$(U_E, V_E) = \frac{1}{\rho f}(\tau^y, -\tau^x), \tag{2}$$

where ρ is the water density (taken to be 1025 kg m^{-3}), and then subtracted these from estimates of the modeled total depth-integrated currents (U, V) to yield the geostrophic flow, assuming

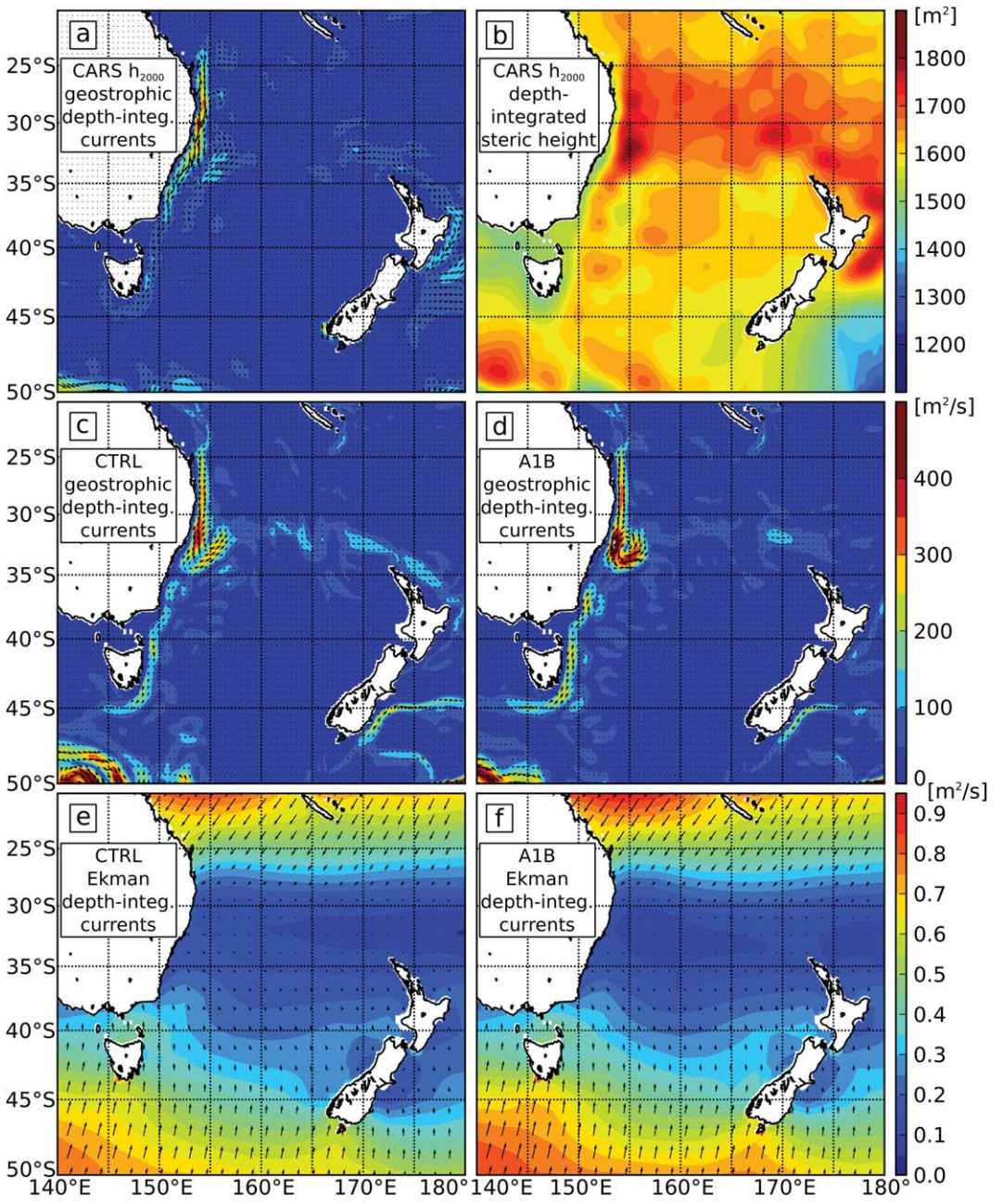

Figure 3. Mean depth-integrated geostrophic and Ekman currents the Tasman Sea. Mean depth-integrated geostrophic currents are shown (a) derived from the CARS depth-integrated steric height (relative to 2000 db, shown in Figure 3b) and from the (c) CTRL and (d) A1B ocean model runs. Ekman transports, calculated from the wind fields used to force the ocean model, are shown for the (e) CTRL and (f) A1B simulations.

$(U, V) = (U_g + U_E, V_g + V_E)$. The Ekman transport indicates northward flow over much of the Tasman Sea and southward flow north of ~30°S (Figure 3e).

The EAC, Tasman Front, and EAC extension are all features evident from both the observed and modeled geostrophic flows (Figures 3a and 3c). The modeled flow appears to represent the EAC quite well, although its separation and retroflexion are stronger than observed. Both the EAC extension and the flow along the Tasman Front appear stronger in the model results than have been observed. It is difficult to unequivocally compare these, however, since the apparently broader and more diffuse observed flows are also defined and limited to some degree by spatial and temporal sampling rates, while the model has its own limitations

albeit that it is highly resolved. Despite these differences, the transports are remarkably similar between the observations and model results.

4.3. Volume Transports Into and Out of the Tasman Sea

Estimates of the volume transports, derived from the CARS steric height field h_{2000} and the model simulated currents, of the primary flows into and out of the Tasman Sea (the EAC, EAC extension, and the Tasman Front) were calculated across the sides of a closed box encompassing the Tasman Sea, following the approach of RG94. The sections were chosen to match RG94 as closely as possible, with direct correspondences for segments AB, BC, DE, and EF (Figure 4, solid lines). However, the eastern edge of the box (CD) in RG94 was defined by a multipart segment that cuts north from point C to a latitude of ~33°S before cutting diagonally across to point D (Figure 4, dashed line). We found it difficult to close the transport budget for flow calculated normal to the diagonal segment and instead chose a segment running directly north from New Zealand to point D (GD, Figure 4). The eastward flow out of the Tasman Sea generally continues north of New Zealand, if we neglect the flow through Cook Strait, and therefore we do not consider that this change in box geometry has significantly impacted the results (Cook Strait transports are <0.2 Sv from both model simulations; observed estimates of the flow through Cook Strait are <1 Sv) [e.g., *Chiswell*, 2000]. We also neglect the flow through the shallow Bass Strait (transports are <0.7 Sv from both model simulations). Finally, we have added a segment (HI) running south of Tasmania in order to monitor flow associated with the Tasman Leakage.

The geostrophic volume transports into and out of the Tasman Sea are broadly consistent between the ocean model CTRL simulation and those observed by RG94 and CARS. The modeled EAC transport into the Tasman Sea across 28°S is within 0.1 Sv of the RG94 value and 1.7 Sv of the CARS value (EF, Figure 4a; 27.4 Sv for RG94, 25.8 Sv for CARS, 27.5 Sv for CTRL). The return flow northward across 28°S is much smaller in the CTRL simulation than is observed (DE, Figure 4a; 18.4 Sv for RG94, 14.8 Sv for CARS, 8.8 Sv for CTRL) and the outflow along the Tasman Front eastward across 173°E is much greater in the CTRL simulation (DG, Figure 4a; 4.1 Sv for RG94, 3.7 Sv for CARS, 12.7 Sv for CTRL). This is due to the fact that the model predicts a more focused eastward flow along the Tasman Front while the observations indicate a broader northeastward flow north of the core of the Tasman Front (compare observed and modeled MDT fields, Figure 2). Nevertheless, the total outflow along the Tasman Front (ED + DG) is within 1.0 Sv of the RG94 value and 3.2 Sv of the CARS value (22.5 Sv for RG94, 18.5 Sv for CARS, 21.5 Sv for CTRL). At the southern boundary of the Tasman Sea, the model projections are similar to the observations. Both the broad northward transport into the Tasman Sea (BC, Figure 4a; 1.0 Sv for RG94, 3.2 Sv for CARS, 2.2 Sv for CTRL) and the focused southward transport out of the Tasman Sea by the EAC extension (AB, Figure 4a; 8.1 Sv for RG94, 9.7 Sv for CARS, 9.7 Sv for CTRL) are consistent with the observed estimates. The Ekman volume transports, typically less than 1 Sv across any section, are always directed into the Tasman Sea and broadly consistent between the model transports and observations (Figure 4b; total inflow of 2.2 Sv for RG94, 1.0 Sv for CTRL). Note that the difference in Ekman transport between RG94 and the CTRL run winds is not due to the difference in time period over which these estimates are calculated. The change in Ekman transport between 1975–1989 and 1990–2002 (calculated from ERA-40 10 m winds) is <10% relative to the earlier period for all sections except AB (in which case it is <20%). The total volume transport into and out of the Tasman Sea from the CTRL simulation is balanced within 1.5 Sv.

We also calculated the flow around the southern tip of Tasmania. The net flow from the model simulation is westward and quite large, although not much larger than the observed estimate from CARS (HI, Figure 4a; 8.1 Sv for CARS, 10.8 Sv for CTRL). This includes the eastward flowing Zeehan Current (~2 Sv) which is trapped along the shelf break as well as the broader westward flow offshore, denoted the Tasman Leakage. The magnitude of this flow is similar to our estimate from CARS (8.1 Sv) and from *Rintoul and Sokolov* [2001] (2001) (8 ± 13 Sv) but is a significant overestimate in comparison to *Speich et al*. [2002] (3 Sv) and *Rosell-Fieschi et al*. [2013] (3.8 ± 1.3 Sv).

4.4. EAC Separation Point

We have estimated the mean path of the EAC, including the location of its separation from the continental shelf, using the technique outlined in *Thompson and Demirov* [2006]. In that study, it was demonstrated that sea level skewness can be used as an indicator of the mean path of western boundary currents. This is due to the preferential pinching off of cyclonic eddies (negative sea level anomaly) and anticyclonic eddies

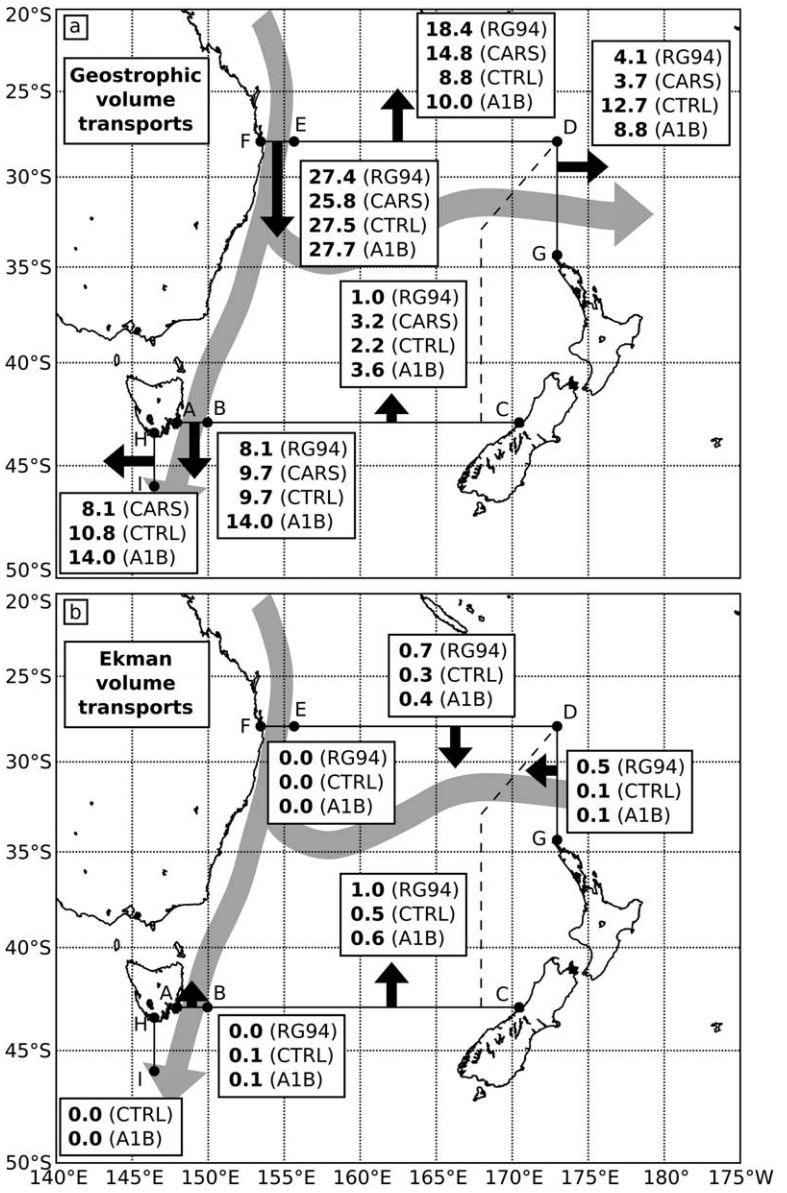

Figure 4. Mean volume transports in to and out of the Tasman Sea. The numbers within each small box indicate the volume transport (in Sv), in the direction indicated by the nearest black arrow, across each segment encompassing the Tasman Sea based on observations (RG94 and CARS) and model simulations for the 1990s (CTRL) and the 2060s (A1B) decades. Both (a) geostrophic and (b) Ekman transports are shown. Arrow lengths represent the approximate transport, relative to the other sections shown. The segments are defined by the following locations: A (148°E, 43°S), B (150°E, 43°S), C (170.5°E, 43°S), D (173°E, 28°S), E (155.7°E, 28°S), F (153.5°E, 28°S), G (173°E, 34.4°S), H (146.5°E, 43.5°S), and I (146.5°E, 46°S). The gray arrows schematically show the underlying mean flow.

(positive sea level anomaly) on the equatorward and poleward sides, respectively, of the mean jet path [e.g., *Boland and Church*, 1981; *Chelton et al.*, 2011].

We have mapped the sea level third moment (m_3, which, for the purposes of defining the mean jet path, is equivalent to skewness) for the observed (Aviso) and CTRL simulation sea levels (Figures 5a and 5b) and identify the mean jet path. There is clear delineation between regions of negative m_3 north and east of the mean path (Figure 5, blue) where cyclonic, or cold-core upwelling, eddies are preferred and regions of positive m_3 (Figure 5, red) where anticyclonic, or warm-core downwelling, eddies are preferred. It is encouraging to note that the mean volume transport tends to flow along the mean jet path (Figure 5, gray arrows) and that the flow along the shelf break, followed by separation and retroflection, is evident in both the observations and the model simulations.

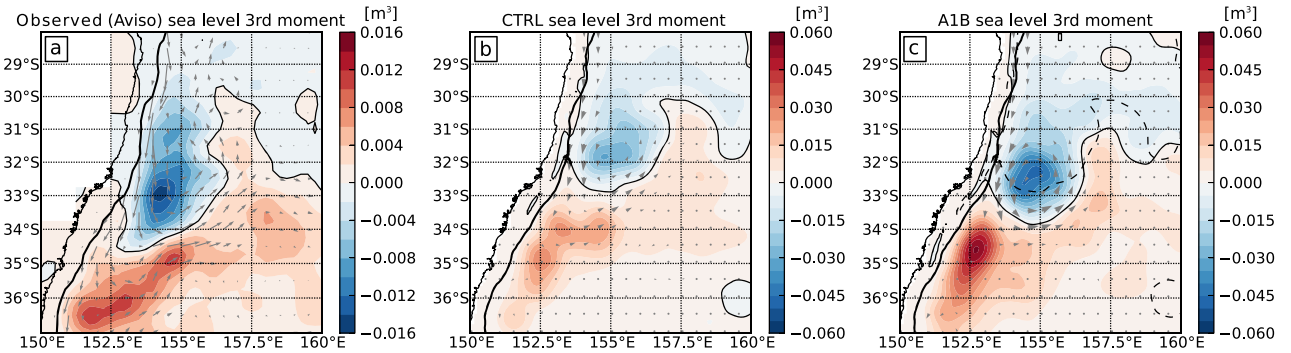

Figure 5. East Australian Current separation and retroflection. Third moment of sea level (m_3, colored contours) and mean volume transport (gray arrows) shown for (a) observations (sea level from Aviso and volume transport derived from CARS mean dynamic topography), (b) CTRL, and (c) A1B model runs. The solid line indicates the zero contour of m_3 (an estimate of the mean jet path) and the thick solid line indicates the 2000 m isobath (taken to represent the shelf break); the dashed line in Figure 5c indicates the zero contour of m_3 from the CTRL simulation. The black dots indicate the location of the EAC separation; the gray dot in Figure 5c indicates the EAC separation point for the CTRL simulation.

The EAC separation point (Figure 5, black dot) was estimated by the intersection between the mean jet path and the 2000 m isobath (Figure 5, thick black line) taken to be a proxy for the shelf break. The estimated separation point from Aviso (152.8°E,33.1°S) is about 75 km further south than previous observations which suggest that it is at Sugarloaf Point (152.5°E, 32.4°S) [*Godfrey et al*., 1980]. It should be noted that we have identified the EAC separation from the shelf break, defined by the 2000 m contour, and not separation from the coastline. In fact, the zero m_3 contour intersects with the coastline very near to Sugarloaf Point. The EAC separation point in the CTRL model simulation is located slightly north of Sugarloaf Point, at (153.5°E, 31.8°S).

4.5. Eddy Kinetic Energy

While the mean circulation in the Tasman Sea is clearly significant, it is also important to examine how well the model reproduces the mesoscale currents. Variability due to mesoscale eddies can be quite large in the region, particularly in the EAC extension region [e.g., *Suthers et al*., 2011]. In western boundary current regions, sea level variance is primarily due to mesoscale eddy variability and a meandering of the jet [*Zlotnicki et al*., 1989; *Thompson and Demirov*, 2006] and can be used as an indicator for eddy kinetic energy. The observed sea level variance, calculated from Aviso, indicates a maximum (0.10–0.12 m^2) around the EAC separation region (Figure 6a). A region of elevated variance ($>$0.05 m^2) extends latitudinally from about 40°S to 25°S and is largest near the coast. This region has a maximum meridional extent of over 10° longitude at the latitude of the EAC separation point ($\sim$33°S), decreasing to about $\sim$5° longitude at the northern and southern extremities. There are also elevated ($\sim$0.02 m^2) levels of sea level variance extending southward from the EAC separation point, along the EAC extension, and extending eastward, along the Tasman Front, and in the Coral Sea north of $\sim$30°S.

The sea level variance estimated by the CTRL simulation is consistent with the observations (Figure 6c). The model simulates the large eddy variability in the EAC separation region, along the EAC extension, Tasman Front, and in the Coral Sea. The model simulation overestimates sea level variance by up to 50%, particularly in the EAC separation region, along the Tasman Front, and in the Coral Sea. This may be partly due to the low-frequency sampling rate of the observations (weekly) in comparison to the model simulation (daily; e.g., error variances in geostrophic velocities estimated from altimeter sea level measurements are between 15% and 50%) [*Leeuwenburgh and Stammer*, 2002].

5. Model Projections for the 2060s

We now turn to the dynamically downscaled model projections for the 2060s from the A1B simulation, and present modeled changes in Tasman Sea volume transports (section 5.1), the location of the EAC separation point (section 5.2), and the changes in eddy kinetic energy (section 5.3) and mean Tasman Sea temperature and salinity (section 5.4).

5.1. Mean Dynamic Topography and Volume Transports

In general, the mean SSHs from the A1B simulation exhibit the same primary features as the mean SSH from the CTRL simulation and the observed MDT (Figure 2d). Clearly evident are the EAC, the EAC extension,

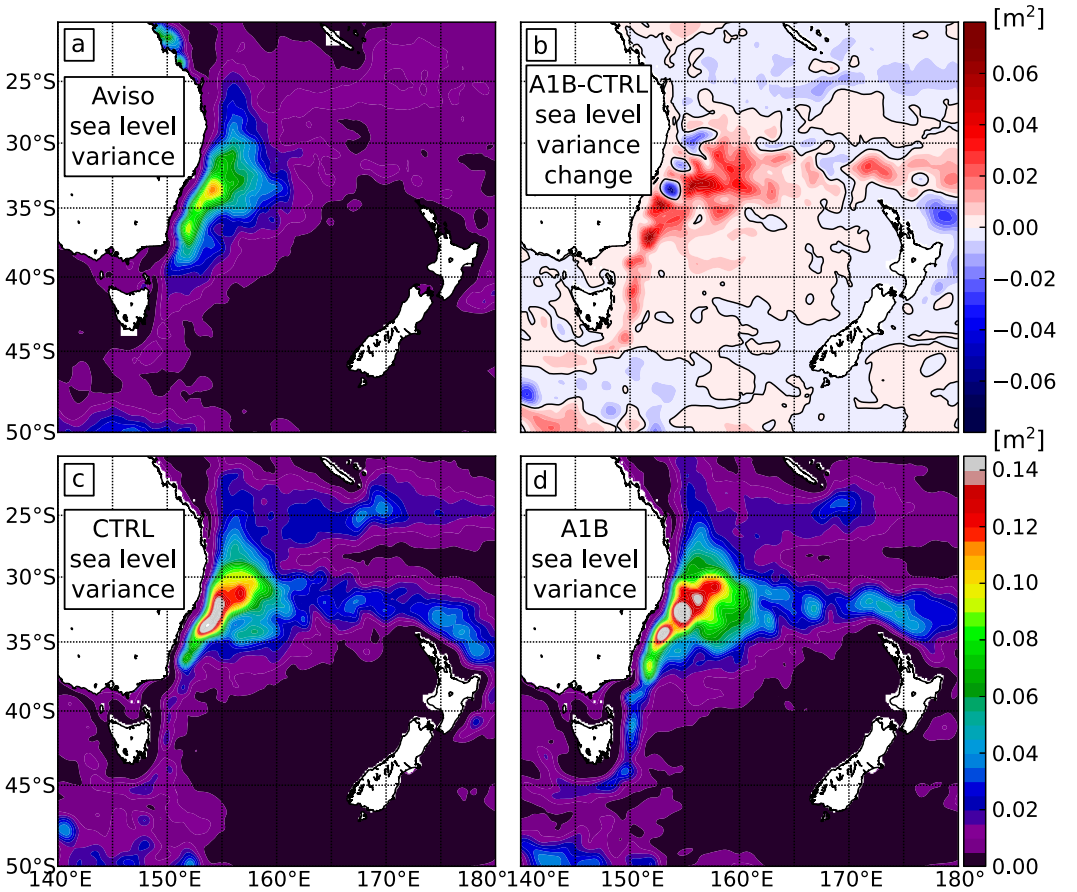

Figure 6. Sea level variance in the Tasman Sea. The variance of sea level is shown for (a) observations (Aviso) and the (c) CTRL and (d) A1B model runs. The change in sea level variance between the CTRL and A1B model runs is shown in Figure 6b.

and the Tasman Front, as well as the EAUC and the ECC along New Zealand's boundary, and the Tasman Leakage off the southern tip of Tasmania. The contours of mean SSH at the EAC separation point appear closer together, possibly indicative of a stronger separation, although the quasi steady anticyclonic eddy at this location also appears stronger and more coherent, indicative of a stronger recirculation after separation. It is difficult to quantify any changes in flow rates from fields of mean SSH and so we now turn to volume transports.

The mean geostrophic volume transports for the A1B simulation (Figure 3d), calculated by removing the Ekman transports (Figure 3f) from the simulated total transports, exhibit the same general pattern as the transports from the CTRL simulation and the observations. The EAC transport, between about 24°S and 32°S, appears to have a similar magnitude as the CTRL simulation while the recirculation, which occurs after separation from the shelf around 33°S, appears much stronger. The transport across the Tasman Sea along the Tasman Front appears weaker while the southward EAC extension appears stronger, as does the Tasman Leakage.

The downscaled future transports through the Tasman Sea, following the A1B simulation, are shown in Figure 4. While there is little change in Ekman transports, the geostrophic transports indicate a redistribution of the flow. The core EAC transport has changed very little (EF, Figure 4a; 27.5 Sv for CTRL, 27.7 Sv for A1B) while the eastward transport out of the Tasman Sea along the Tasman Front decreases by 3.9 Sv (DG, Figure 4a; 12.7 Sv for CTRL, 8.8 Sv for A1B) and the southward transport out of the Tasman Sea by the EAC extension increases by 4.3 Sv (AB, Figure 4a; 9.7 Sv for CTRL, 14.0 Sv for A1B), essentially closing the transport budget. Over the remainder of the sections, the small increase in transport out of the Tasman Sea at the northern boundary (DE, Figure 4a; 8.8 Sv for CTRL, 10.0 Sv for A1B) is nearly balanced (within ~1 Sv) by the small increase in transport into the Tasman Sea at the southern boundary (BC, Figure 4a; 2.2 Sv for CTRL, 3.6 Sv for A1B) and the

slightly increased input by the EAC. The Tasman Leakage, i.e., the westward flow past the southern tip of Tasmania, is projected to increase by 4.8 Sv (HI, Figure 4a; 10.8 Sv for CTRL, 14.0 Sv for A1B).

The variability in the flow is high in this region, primarily due to eddy activity, and it was of concern how significant the changes in transport were across the sections quoted above. We performed a paired *t* test [e.g., *Devore*, 1999] on the 9 year, monthly time series of geostrophic transports across each segment shown in Figure 4 to test if the mean transports were significantly different between the CTRL and A1B runs. Serial correlation of the monthly series was taken into account by estimating the effective sample sizes and number of degrees of freedom following the technique outlined in *Zwiers and von Storch* [1995]. We found that simulated changes in the mean transport are significantly different from zero at the 5% level across AB (EAC extension) and at the 1% level across DG (Tasman Front) and HI (Tasman Leakage). The changes in mean transport across the other sections were not significant at a reasonable level of confidence.

5.2. EAC Separation Point

We estimated the mean path of the EAC flow, including the location of its separation point, for the A1B simulation (Figure 5c). As above, the estimated mean path follows well the path of greatest mean transport (Figure 5c, compare black line and gray arrows). The separation point, defined as the intersection between the mean jet path and the 2000 m isobath, is estimated to be (153.2°E, 32.6°S). This location is 0.8° latitude further south and 0.3° longitude further west than the location estimated from the CTRL simulation. This corresponds to a 93.4 km southward (poleward) shift of the EAC separation point along the shelf break.

5.3. Eddy Kinetic Energy

We calculated the sea level variance for the A1B simulation (Figure 6d). The sea level variance has broadly the same pattern as for the observations (Figure 6a) and the CTRL run (Figure 6c), namely a peak near the EAC separation point and elevated levels along the EAC extension, Tasman Front, and in the Coral Sea. However, the A1B simulation results in a larger sea level variance (up to a factor of two) in the EAC extension region and in the interior of the Tasman Sea (Figure 6b). This may be due to enhanced eddy activity in these regions. The A1B simulation also produced enhanced sea level variance immediately east of the EAC separation zone and along the Tasman Front, as well as a possible southward shift of the entire pattern by about 1° of latitude.

5.4. Temperature and Salinity Changes

We have estimated the changes in mean temperature and salinity in the Tasman Sea with a focus on the surface changes along the continental shelf (Figure 7). Temperature is projected to increase throughout the entire Tasman Sea, with larger magnitude near the surface: 0.5–3°C at the surface (Figure 7a), 0.5–2°C at 200 m (Figure 7b), and 0–0.5°C at 1000 m (Figure 7c). While surface changes are less than 2°C over most of the domain, consistent with Global Climate Model projections of 1–1.5°C for this region [*Meehl et al*., 2007], there is a "Tasman Sea hot spot," centered near (160°E, 36°S) and roughly circular in extent with ∼15° diameter, where sea surface temperature (SST) changes are in excess of 2°C. These elevated changes in SST also extend to the Australian coast at roughly the location of the EAC separation indicating that these SST changes may be due to increased warm water advection into the Tasman Sea by an enhanced EAC recirculation at the separation point (see section 5.1). There is also a signature of elevated temperature change at both the 200 m and 1000 m depths collocated with the enhanced quasi-stationary anticyclonic EAC recirculation eddy (155°E, 33°S).

Salinity changes are more heterogeneous in space, both horizontally and vertically, than the temperature changes. At the surface, salinity is decreased by approximately 0.2 PSU in the core of the EAC and by 0.1–0.2 PSU southwest of New Zealand, while it is increased by up to 0.1 PSU in a band running east and northeast of Tasmania (Figure 7d). At 200 m depth, salinity is decreased by 0–0.1 PSU over most of the domain (up to 0.15 PSU along the west coast of New Zealand) and increases slightly (∼0.05 PSU) southeast of Tasmania (Figure 7e). At 1000 m depth, there is an overall freshening by ∼0.05 PSU over the whole domain (Figure 7f). These changes are broadly consistent with the warming and freshening of intermediate waters seen in historical observations [*Bindoff and Church*, 1992; *Wong et al*., 1999].

The temperature and salinity properties of the surface waters along the continental shelf break are projected to change significantly between the 1990s and 2060s. The surface temperature and salinity along the line shown in Figure 7a (black line) for both the CTRL and A1B runs are provided in Figure 8a, color-coded by

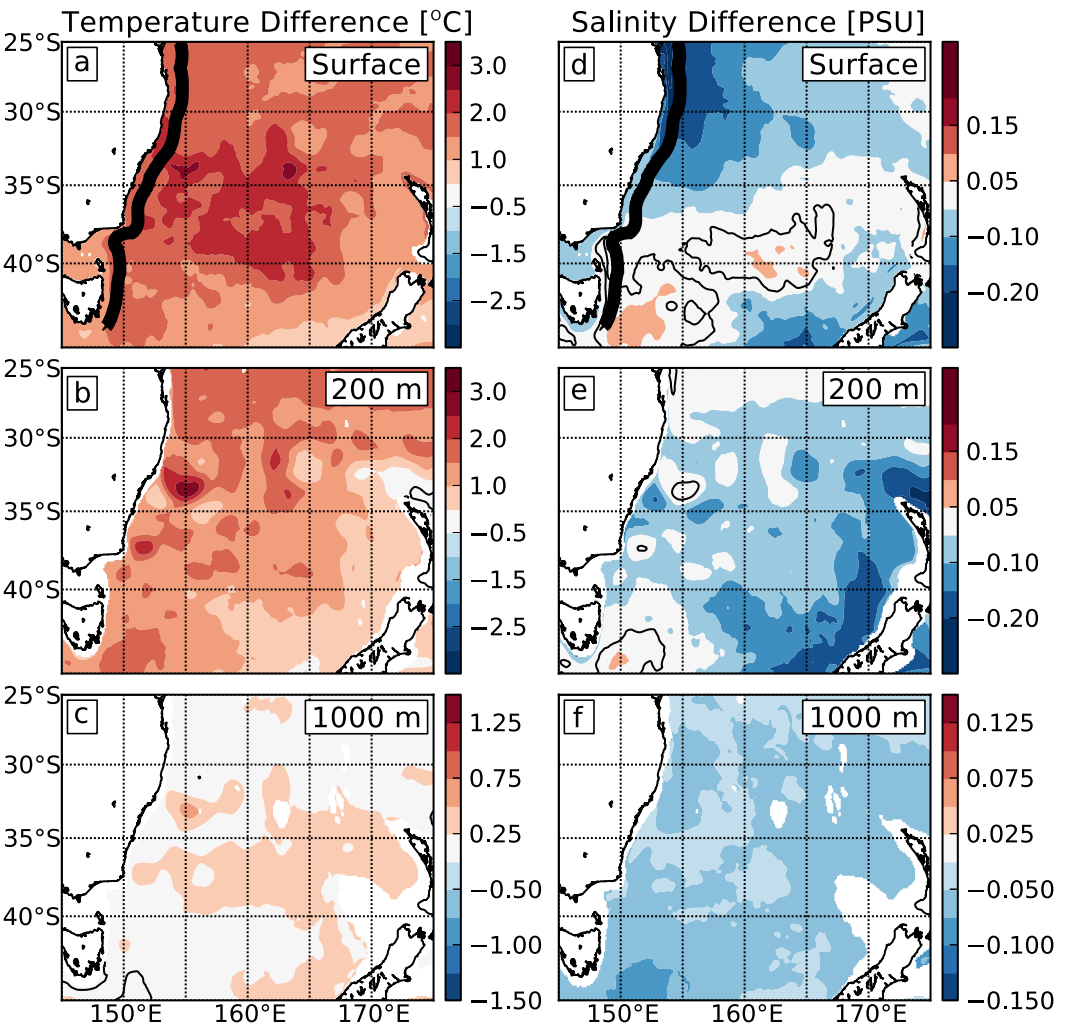

Figure 7. Projected changes in mean temperature and salinity. The difference between the A1B scenario and CTRL simulations of (a–c) mean temperature and (d–f) salinity is shown for (a and d) the surface, (b and e) 200 m depth, and (c and f) 1000 m depth. The black line shows the section used in Figure 8. Note areas of white indicate changes within (a and b) ±0.5°C, (c) ±0.25°C, (d and e) ±0.05 PSU, and (f) ±0.025 PSU.

latitude. The line is meant to follow the continental shelf break, but since the dynamical downscaling afforded by OFAM is not designed for the continental shelf [e.g., *Oliver and Holbrook*, 2014] the line is in fact the 200 m contour, between 43.8°S and 25°S, shifted 1° longitude to the east (away from the shelf into the deep ocean where OFAM tends to perform very well). At higher latitudes (44°S–41°S, east of Tasmania), there is a projected future warming (∼+2°C) and salinification (∼+0.05 PSU) consistent with the historical past changes observed at Maria Island (148.23°E, 42.6°S) [*Ridgway*, 2007]. The salinification decreases as one moves equatorward along the line so that north of Bass Strait (38–39°S) there is a freshening of the surface waters (Figure 8c) while the temperature increase remains roughly constant over all latitudes (Figure 8b).

6. Interpretation: Sverdrup Stream Function and Island Rule Transports

In the present study, we have focused on the mean circulation in the Tasman Sea: the EAC, the EAC Extension, and the Tasman Front. In particular, we are interested in the relative strengths (i.e., volume transports) of these features, as well as the location of the EAC separation point which demarcates them. In order to estimate how these features respond to changes in the large-scale wind forcing, we take an approach based on the *Godfrey* [1989] Island Rule. The Island Rule is a generalization of the Sverdrup stream function to

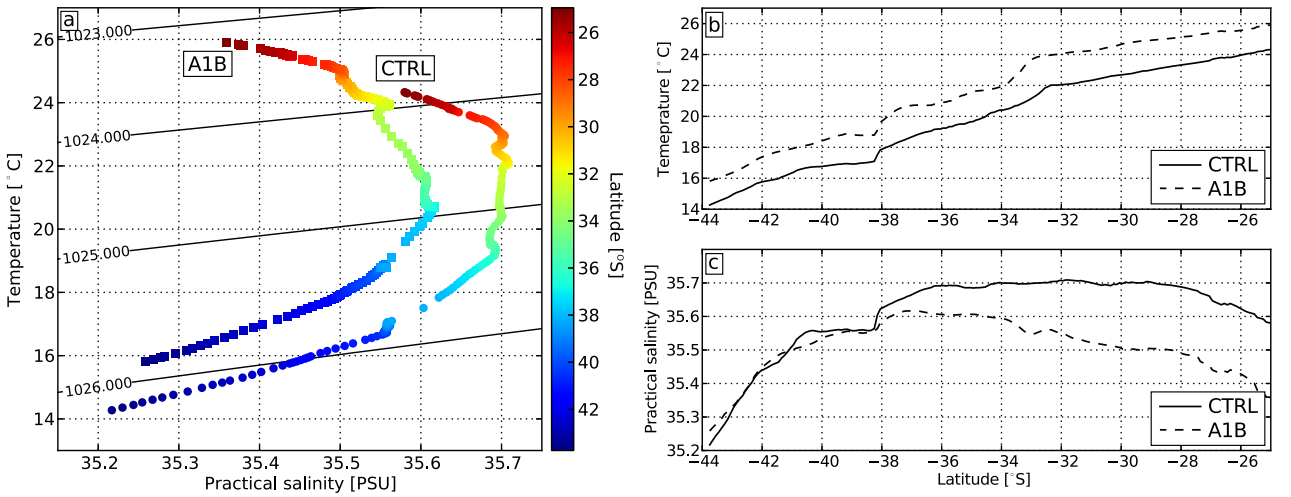

Figure 8. Temperature and salinity properties along the continental shelf of southeastern Australia. (a) The mean surface temperature and salinity are shown on a T-S diagram as a function of latitude (colors) along the line shown in Figure 7 for the CTRL run (circles) and the A1B run (squares). Contours show density with labels in kg m^{-3}. The mean surface (b) temperature and (c) salinity along this line are shown as functions of latitude.

include the effect of islands, such as New Zealand, which lie between the primary eastern and western boundaries of a basin [see also *Wajsowicz*, 1993; *Pedlosky et al*., 1997]. It is a general approach that facilitates estimates of the volume transport of western boundary currents.

6.1. Theory

The barotropic Sverdrup stream function $\psi(x, y)$ for the ocean can be calculated by zonally integrating the depth-integrated meridional flow V ($m^2\ s^{-1}$) following the definition $\partial\psi/\partial x = V$, given an initial condition for ψ at the eastern boundary. The meridional flow V is given by the Sverdrup balance:

$$\beta V = \frac{1}{\rho H}\nabla \times \tau \tag{3}$$

where β is the meridional derivative of the Coriolis parameter ($m^{-1}\ s^{-1}$), ρ is water density (kg m^{-3}), H is depth (m), and τ is the surface wind stress vector (N m^{-2}). This relationship implies that a positive wind stress curl leads to equatorward volume transport (Sverdrup transport). In order to close the circulation, and due to friction and the β-effect, the Sverdrup transport must be balanced by an intense return (poleward) flow at the western boundary: the western boundary current (WBC) [e.g., *Gill*, 1982; *Samelson*, 2011]. The Island Rule [*Godfrey*, 1989] is an extension of Sverdrup theory which calculates the flow around islands, by integrating the wind stress along a particular path encompassing the island, and incorporating the influence of such islands into the Sverdrup stream function.

The separation of WBCs from the western boundary may be interpreted using the Sverdrup balance. Sharp meridional gradients in wind stress curl lead to convergence or divergence of the meridional flow and thus, by continuity, zonal flows. The steady state depth-integrated continuity equation for an incompressible fluid gives $\partial U/\partial x = -\partial V/\partial y$, where U is the depth-integrated zonal fluid velocity, and so convergence at the western boundary (i.e., divergence in the interior of the basin; $\partial V/\partial y < 0$) leads to an eastward flow away from the boundary. This eastward flow may lead to separation or partial separation of the western boundary current [e.g., *Tilburg et al*., 2001; *Bostock et al*., 2006].

A schematic of this process, a simple representation of the mean circulation at the western boundary of a southern hemisphere ocean basin, is provided in Figure 9. Wind stress curl is positive over the South Pacific subtropics and midlatitudes (Figure 9a) leading to equatorward flow (due to the Sverdrup balance and neglecting any corrections due to the Island Rule) over the entire basin interior and poleward flow along the western boundary (Figure 9c). North of some critical latitude y_c the wind stress curl is large relative to its value south of y_c. Therefore, the boundary current is stronger for $y > y_c$ (the "western boundary current

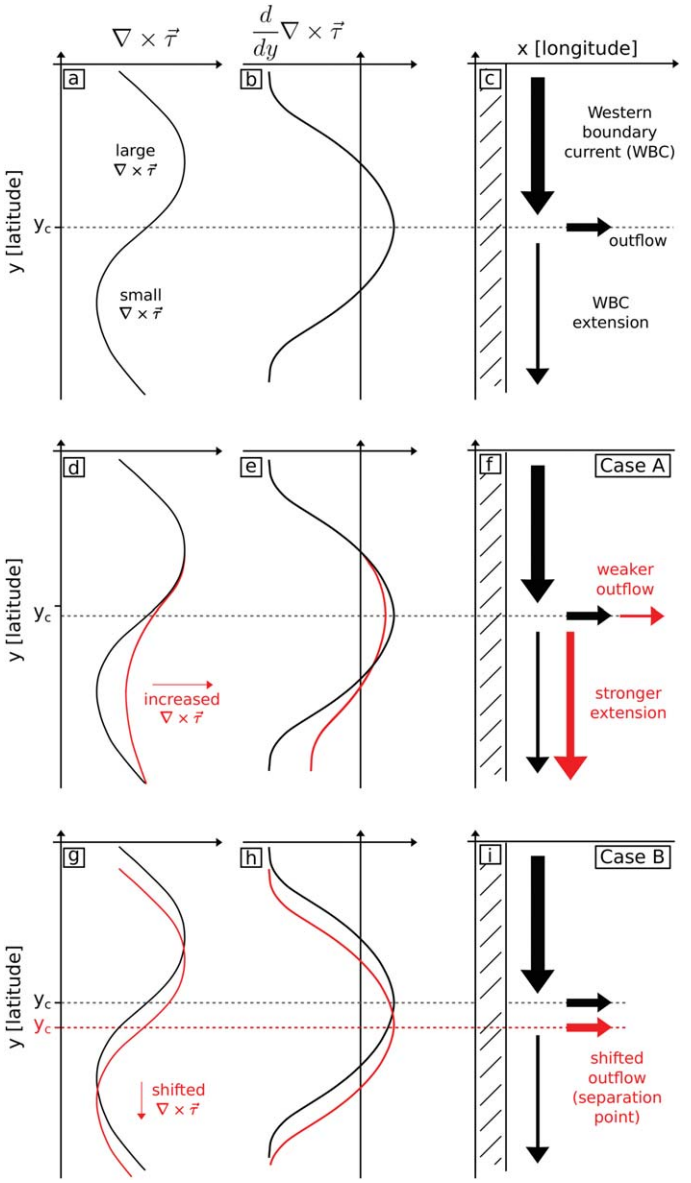

Figure 9. Schematic of western boundary flow, in the southern hemisphere, due to meridional variations in wind stress curl. A schematic of (a) southern hemisphere midlatitude wind stress curl, and (b) its meridional derivative, which lead to (c) the boundary flows and zonal outflows indicated by the arrows. Also shown are the changes in circulation (red arrows) due to (Case A; d–f) an increase in high-latitude wind stress curl and (Case B; g–i) a poleward shift in the wind stress pattern (red lines).

(WBC)") and weaker for $y < y_c$ (the "WBC extension") leading to convergence at $y = y_c$. Continuity requires a zonal flow to balance this convergence and so there must be an eastward flow along $y = y_c$ (the "outflow").

Consider the consequence of two possible changes to the simple flow schematic shown in Figure 9. First, consider the Case A where the wind stress curl poleward of the separation point ($y < y_c$) is increased while the wind stress curl equatorward of the separation point ($y > y_c$) remains unchanged (Figure 9d). The consequence of this is that the WBC transport ($y > y_c$) remains the same while the transport in the WBC extension is enhanced due to the greater wind stress curl over $y < y_c$ (Figure 9f). An additional consequence is that the convergence at $y = y_c$ is reduced, leading to a reduced outflow (Figure 9f). Second, consider the Case B where the entire meridional distribution of wind stress curl is shifted southward (Figure 9g). The consequence of this is that the WBC separation point (the point of maximum convergence, $y = y_c$) shifts while the strengths of the WBC, WBC extension, and the outflow remain the same (Figure 9i).

6.2. Application to CTRL and A1B Surface Wind Stress Forcing

The zonally averaged South Pacific wind stress curl, calculated from the model forcing fields for the CTRL run, is qualitatively consistent with this simple schematic (Figure 10a, black line). Specifically, the wind stress curl is larger on the equatorward side of the midlatitudes (30°S) than on the poleward side (35–40°S), as in the schematic (Figure 9a). The zonally averaged wind stress curl from the A1B run (Figure 10a, red line) exhibits a similar pattern albeit with increased values at higher latitudes (poleward of 35°S). Therefore, we anticipate a response of the WBC transports following the concepts presented in Case A outlined above. (Note that we have subsampled the 0.1° OFAM forcing fields every 2.5° in latitude and longitude, corresponding to the original coarse-resolution forcing fields, in order to avoid discontinuities in higher order derivatives. We then interpolated the zonally averaged fields onto a 0.1° grid using a cubic spline in order to ensure continuity.)

The depth-integrated stream function for the South Pacific, calculated from the Sverdrup relation and the Island Rule given the coarse 2.5° resolution CTRL run forcing fields and an initial value of $\psi = 0$ on the

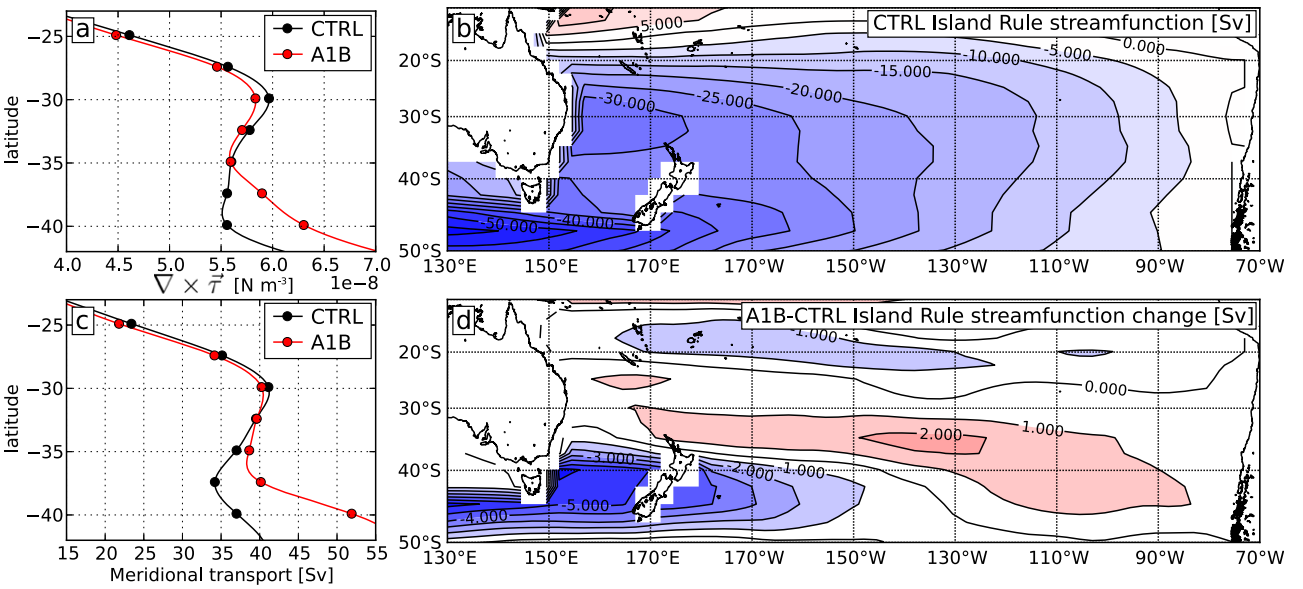

Figure 10. Depth-integrated wind-driven circulation according to the *Godfrey* [1989] Island Rule. (a) The zonally averaged South Pacific wind stress curl, shown for the CTRL (black) and A1B (red) runs. Both the coarse 2.5° resolution (dots) and the fine 0.1° interpolated fields (lines) are shown. (b) The depth-integrated stream function (contours shown in Sv), calculated from the CTRL surface wind stress fields according to the Island Rule, for the South Pacific Ocean and (d) the change (in Sv) between the stream functions derived from the CTRL and A1B wind stress fields. (c) The meridional transport in the western boundary current, as a function of latitude along the coast of Australia, calculated from the Island Rule stream functions for the CTRL (black) and A1B (red) forcing fields.

eastern boundary, shows a clear South Pacific subtropical gyre (Figure 10b). There is northward flow over much of the interior South Pacific, westward flow in the tropics leading to a bifurcation at the Australian mainland, and the formation of the WBC poleward of 18°S. There is even a partial separation of the WBC, with some eastward flow, around 35°S. The remainder of the WBC flow continues south along the Australian coastline. The South Pacific subtropical gyre estimated by this stream function is consistent—in shape, magnitude, and Island Rule values for Australia and New Zealand—with previous estimates [*Godfrey*, 1989; *Cai et al*., 2005; *Cai*, 2006; *Godfrey and Dunn*, 2010; *Hill et al*., 2008, 2011].

Meridional flow was estimated by calculating $V = \partial\psi/\partial x$ using a first difference in x and the transport in the WBC was calculated using the value of V in the first grid cell east of the Australian mainland (Figure 10c). This follows under the assumption that the transport in the WBC at each latitude exactly balances the total Sverdrup transport in the gyre interior at that latitude. Over the domain of interest here (25°S–40°S), there is a peak in meridional transport of ∼40 Sv around 30°S (Figure 10c) (corresponding to the core of the EAC; an overestimate of ∼40%) [see *Ridgway and Godfrey*, 1994], reduced transport of 35–40 Sv over the latitude range 30°S–40°S (corresponding to the EAC extension), and maximum convergence of the meridional flow occurring over the range ∼32.5–35°S, which by continuity will lead to a zonal outflow at these latitudes (the Tasman Front). The estimated southward meridional flow across the Tasman Sea (integrated across the basin between Australia and New Zealand) is 18.3 Sv (at 39.9°S) and 16.3 Sv (at 42.4°S) which is consistent with previous Island Rule estimates of 10–20 Sv [*Hill et al*., 2008].

The change between the depth-integrated stream functions estimated from the CTRL and A1B forcing fields is shown in Figure 10d. The change is dominated by a strengthening (by up to 5 Sv) of the subtropical gyre in the Tasman Sea and just east of New Zealand. There is also a slight weakening (∼2 Sv) of the gyre in the interior of the South Pacific Ocean. The peak in meridional transport of the WBC is of similar magnitude (∼40 Sv) to that derived from the CTRL forcing fields and lies at the same latitude (30°S; Figure 10c). The meridional transport at higher latitudes, corresponding to the EAC extension, is enhanced by the increased wind stress curl south of y_c, and the zonal outflow along ∼32.5–35°S (the Tasman Front) is reduced due to the reduced convergence of meridional flow $(\partial V/\partial y)$. This is consistent with the projected changes in geostrophic transports derived from the dynamically downscaled OFAM simulation (Figure 4), where the core EAC varies little in intensity north of y_c but the flow out of the Tasman Sea is redistributed such that the intensity of the EAC extension is enhanced and the flow along the Tasman Front is reduced. While the

magnitude of the transports derived from the Island Rule stream function are not wholly consistent with those from OFAM, the general meridional pattern and the predicted redistribution of transport, due to the change in wind stress curl, is consistent. In fact, it is remarkable that this relatively simple, linear theory is able to capture these changes.

The change in latitude of maximum convergence (y_c, i.e., the separation point), according to Sverdrup theory, is not consistent between the Sverdrup model estimates and OFAM. The maximum convergence in the CTRL Sverdrup stream function lies between 30°S and 37.5°S, while for the A1B scenario Sverdrup stream function it lies between 30°S and 35°S (the steepest part of the lines in Figure 10c). While the OFAM simulations project a ~1° latitude poleward shift in the EAC separation point (section 4.4; Figure 5), the Sverdrup stream functions predict, if anything, an equatorward shift in the average position. Therefore, the simple linear theory is unable to capture the southward shift in the EAC separation point, which will be discussed further in the next section.

7. Discussion

In this paper, we have examined the response of the mean western boundary current circulation of the South Pacific subtropical gyre, using a dynamically downscaled model projection of climate change under the A1B carbon emissions scenario. The downscaled projections, from the Ocean Forecasting Australia Model (OFAM) in the Tasman Sea region, indicate that from the 1990s to the 2060s the volume transport in the East Australian Current (EAC) extension, which carries warm water poleward of the mean separation point from the east Australian coast, will increase (by 4.3 Sv) at the expense of the outflow along the Tasman Front (decrease by 2.7 Sv). Interestingly, the transport in the core of the EAC, which represents the mean flow equatorward of the mean separation point, is projected to change very little (increase by 0.2 Sv). Our findings extend the "spin-up of the gyre" paradigm, in which the entire South Pacific subtropical gyre or Southern Hemisphere supergyre increases in strength over time [i.e., *Roemmich et al*., 2007; *Cai*, 2006], in that we demonstrate that substantive changes in the western boundary current transports are projected to only occur poleward of the EAC separation point. These projected changes in the circulation are consistent with mechanisms that might explain the recent observations of increased upper ocean temperature and salinity in the Tasman Sea "hot spot."

The projected mean circulation changes in the Tasman Sea are consistent with predictions from a simple linear, barotropic model based on the Sverdrup transport and *Godfrey* [1989] Island Rule. Utilizing the projected South Pacific wind stress fields, the simple model captures the meridional distribution of change in western boundary current transport, including negligible change in the core EAC transport at 30°S and an increase (by up to 5 Sv) of EAC extension transport between 32.5°S and 37.5°S at the expense of the eastward zonal outflow along the Tasman Front. We note that the simple model does not accurately capture the magnitude of the transports in the western boundary currents—in particular the EAC extension is significantly overestimated and the magnitude of change at latitudes poleward of 40°S is far too large. This is not surprising as the model does not capture the complex dynamics of the western boundary current. It does nevertheless demonstrate the fundamental dynamic balance, leading to enhanced high-latitude western boundary current transport that appears to be satisfied by the complex eddy-resolving OFAM projections, notably elevated eddy activity in the EAC extension as indicated by sea level variance.

We also tested if the enhanced poleward transport in the EAC extension was accompanied by a change in the mean separation point of the EAC from the western boundary. It was found that in the dynamically downscaled model projections the separation point had shifted nearly 100 km poleward along the continental shelf break from the 1990s to the 2060s, consistent with the findings of *Matear et al*. [2013]. However, the linear Island Rule model does not capture this change in separation point in the barotropic stream function. There are two possible reasons for this. First, the resolution of the coarse forcing fields are 2.5° in latitude and longitude, and therefore it is difficult, if not impossible, to detect a southward shift of less than 1° of latitude. The second, and possibly more likely reason, is that the mean location of the separation point is governed by baroclinic, eddy-rich dynamics, which makes it not surprising that the simple linear model does not explain such changes. Furthermore, the separation point of a western boundary current is sensitive to the relative strength of the adjacent flow. *Matano* [1993] demonstrated that the separation point of the Brazil Current (the WBC of the South Atlantic) is sensitive to the strength of the Malvinas Current, which

flows northward along the continental shelf south of the separation point. Hence, the change in transport of the EAC extension may actually influence the location of EAC separation.

While examining changes to the mean circulation is helpful for addressing the greater questions surrounding marine climate change in the Tasman Sea, in the EAC separation and EAC extension regions the eddy kinetic energy due to mesoscale variability is at least as large, if not larger, than the energy associated with the steady, mean flow. It is remarkable that the simple linear model estimates the same change in mean flow, due to changes in the wind-driven circulation that was estimated from the eddy-resolving ocean model. But it is notable that these transport changes occur not in the steady circulation but in the mesoscale eddy field, and that the linear model does not capture the change in EAC separation point. Hence, while the simple linear model is useful as it provides us with a fundamental dynamical balance which must be met by the ocean circulation, this balance is nevertheless met by nonlinear dynamics not explicitly included in simple linear model (namely, mesoscale eddies). Future work will focus on projected changes to the eddy field and how these changes are linked to corresponding changes in the marine climate (i.e., warming, salinification, and stratification), as well as whether there are any two-way feedbacks between them. For example, changes to the upper ocean stratification may influence the barotropic and baroclinic instabilities responsible for eddy formation and stability in the EAC extension region. Furthermore, it is of great interest to understand whether the projected warming in the Tasman Sea "hot spot" is mostly due to projected changes in Tasman Sea mean circulation, or if the bulk of this warming is due to other processes.

Acknowledgments

The authors would like to acknowledge funding from the Australian Research Council Super Science Fellowship (grant FS110200029). The authors would like to acknowledge Richard Matear and Matthew Chamberlain of CSIRO Marine and Atmospheric Research (Hobart, Australia) for helpful discussions and for providing the OFAM model output; the authors would also like to acknowledge Bo Qiu of the University of Hawaii for additional helpful discussions. This paper makes a contribution to the objectives of the ARC Centre of Excellence for Climate System Science (ARC CoE CSS) and the CLIVAR-endorsed Southwest Pacific Ocean Circulation and Climate Experiment (SPICE). The altimeter products were produced by Ssalto/Duacs and distributed by Aviso, with support from Cnes (http://www.aviso.oceanobs.com/duacs/).

References

Bindoff, N. L., and J. A. Church (1992), Warming of the water column in the southwest Pacific Ocean, *Nature*, *357*(6373), 59–62.

Boland, F. M., and J. A. Church (1981), The East Australian current 1978, *Deep Sea Res., Part A*, *28*(9), 937–957.

Bostock, H. C., B. N. Opdyke, M. K. Gagan, A. E. Kiss, and L. K. Fifield (2006), Glacial/interglacial changes in the East Australian current, *Clim. Dyn.*, *26*(6), 645–659.

Brassington, G. B., N. Summons, and R. Lumpkin (2011), Observed and simulated Lagrangian and eddy characteristics of the East Australian Current and the Tasman Sea, *Deep Sea Res., Part II*, *58*(5), 559–573.

Cai, W. (2006), Antarctic ozone depletion causes an intensification of the Southern Ocean supergyre circulation, *Geophys. Res. Lett.*, *33*, L03712, doi:10.1029/2005GL024911.

Cai, W., G. Shi, T. Cowan, D. Bi, and J. Ribbe (2005), The response of the Southern Annular Mode, the East Australian Current, and the southern mid-latitude ocean circulation to global warming, *Geophys. Res. Lett.*, *32*, L23706, doi:10.1029/2005GL024701.

Chamberlain, M. A., C. Sun, R. J. Matear, M. Feng, and S. J. Phipps (2012), Downscaling the climate change for oceans around Australia, *Geosci. Model. Dev. Discuss*, *5*, 425–458.

Chelton, D. B., M. G. Schlax, and R. M. Samelson (2011), Global observations of nonlinear mesoscale eddies, *Prog. Oceanogr.*, *91*(2), 167–216.

Chiswell, S. M. (2000), The Wairarapa coastal current, *N. Z. J. Mar. Freshwater Res.*, *34*(2), 303–315.

Church, J. A. (1987), East Australian Current adjacent to the Great Barrier Reef, *Aust. Mar. Freshwater Res.*, *38*(6), 671–683.

Condie, S. A., and J. R. Dunn (2006), Seasonal characteristics of the surface mixed layer in the Australasian region: Implications for primary production regimes and biogeography, *Mar. Freshwater Res.*, *57*(6), 569–590.

Denham, R. N., and F. G. Crook (1976), The Tasman Front, *N. Z. J. Mar. Freshwater Res.*, *10*(1), 15–30.

Devore, J. L. (1999), *Probability and Statistics for Engineering and the Sciences*, 775 pp., Duxbury, Pacific Grove, California, USA.

Dunn, J. R., and K. R. Ridgway (2002), Mapping ocean properties in regions of complex topography, *Deep Sea Res., Part I*, *49*(3), 591–604.

Gill, A. E. (1982), *Atmosphere-Ocean Dynamics*, Academic, San Diego, Calif.

Godfrey, J. S. (1989), A Sverdrup model of the depth-integrated flow for the world ocean allowing for island circulations, *Geophys. Astrophys. Fluid Dyn.*, *45*(1–2), 89–112.

Godfrey, J. S., and J. R. Dunn (2010), Depth-integrated steric height as a tool for detecting non-Sverdrup behavior in the global ocean, *J. Mar. Res.*, *68*(3–4), 387–412.

Godfrey, J. S., G. R. Cresswell, T. J. Golding, A. F. Pearce, and R. Boyd (1980), The separation of the East Australian Current, *J. Phys. Oceanogr.*, *10*(3), 430–440.

Heath, R. A. (1985), A review of the physical oceanography of the seas around New Zealand—1982, *N. Z. J. Mar. Freshwater Res.*, *19*(1), 79–124.

Hill, K., S. R. Rintoul, R. Coleman, and K. R. Ridgway (2008), Wind-forced low frequency variability of the East Australian Current, *Geophys. Res. Lett.*, *35*, L08602, doi:10.1029/2007GL032912.

Hill, K., S. R. Rintoul, K. R. Ridgway, and P. R. Oke (2011), Decadal changes in the South Pacific western boundary current system revealed in observations and ocean state estimates, *J. Geophys. Res.*, *116*, C01009, doi:10.1029/2009JC005926.

Holbrook, N. J., and N. L. Bindoff (1997), Interannual and decadal temperature variability in the southwest Pacific Ocean between 1955 and 1988, *J. Clim.*, *10*(5), 1035–1049.

Holbrook, N. J., I. D. Goodwin, S. McGregor, E. Molina, and S. B. Power (2011), ENSO to multi-decadal time scale changes in East Australian Current transports and Fort Denison sea level: Oceanic Rossby waves as the connecting mechanism, *Deep Sea Res., Part II*, *58*(5), 547–558.

IOC, SCOR, and IAPSO (2010), The international thermodynamic equation of seawater—2010: Calculation and use of thermodynamic properties, *Intergovernmental Oceanographic Commission [in English], Manuals and Guides 56*, 196 pp., UNESCO.

Johnson, C. R., et al. (2011), Climate change cascades: Shifts in oceanography, species' ranges and subtidal marine community dynamics in eastern Tasmania, *J. Exp. Mar. Biol. Ecol.*, *400*(1), 17–32.

Last, P. R., W. T. White, D. C. Gledhill, A. J. Hobday, R. Brown, G. J. Edgar, and G. Pecl (2010), Long-term shifts in abundance and distribution of a temperate fish fauna: A response to climate change and fishing practices, *Global Ecol. Biogeogr.*, *20*, 58–72.

Leeuwenburgh, O., and D. Stammer (2001), Uncertainties in altimetry-based velocity estimates, *J. Geophys. Res.*, *107*(C10), 1–16.
Matano, R. P. (1993), On the separation of the Brazil Current from the coast, *J. Phys. Oceanogr.*, *23*, 79–79.
Matear, R. J., M. A. Chamberlain, C. Sun, and M. Feng (2013), Climate change projection of the Tasman Sea from an eddy-resolving ocean model, *J. Geophys. Res.*, *118*, 2961–2976.
Meehl, G. A., et al. (2007), *Global climate projections, in Climate Change 2007: The Physical Science Basis. Contribution of Working Group I to the Fourth Assessment Report of the Intergovernmental Panel on Climate Change*, edited by S. Solomon et al., pp. 747–845, Cambridge Univ. Press, Cambridge, U. K.
Oke, P. R., G. B. Brassington, D. A. Griffin, and A. Schiller (2008), The Bluelink ocean data assimilation system (BODAS), *Ocean Modell.*, *21*(1–2), 46–70.
Oliver, E. C. J., and N. J. Holbrook (2014), A statistical method for improving continental shelf and near-shore marine climate predictions, *J. Atmos. Oceanic Technol.*, *31*, 216–232.
Oliver, E. C. J., S. J. Wotherspoon, and N. J. Holbrook (2014), Projected Tasman Sea extremes in sea surface temperature through the 21st Century, *J. Clim.*, *27*(5), 1980–1998.
Pedlosky, J., L. J. Pratt, M. A. Spall, and K. R. Helfrich (1997), Circulation around islands and ridges, *J. Mar. Res.*, *55*(6), 1199–1251.
Ridgway, K. R. (2007), Long-term trend and decadal variability of the southward penetration of the East Australian Current, *Geophys. Res. Lett.*, *34*, L13613, doi:10.1029/2007GL030393.
Ridgway, K. R., and J. R. Dunn (2003), Mesoscale structure of the mean East Australian Current System and its relationship with topography, *Prog. Oceanogr.*, *56*(2), 189–222.
Ridgway, K. R., and J. R. Dunn (2007), Observational evidence for a southern hemisphere oceanic supergyre, *Geophys. Res. Lett.*, *34*, L13612, doi:10.1029/2007GL030392.
Ridgway, K. R., and J. S. Godfrey (1994), Mass and heat budgets in the East Australian Current: A direct approach, *J. Geophys. Res.*, *99*(C2), 3231–3248.
Ridgway, K. R., J. R. Dunn, and J. Wilkin (2002), Ocean interpolation by four-dimensional weighted least squares-application to the waters around Australasia, *J. Atmos. Oceanic Technol.*, *19*(9), 1357–1375.
Rintoul, S. R., and S. Sokolov (2001), Baroclinic transport variability of the Antarctic Circumpolar Current south of Australia (WOCE repeat section SR3), *J. Geophys. Res.*, *106*(C2), 2815–2832.
Rio, M., S. Guinehut, and G. Larnicol (2011), New CNES-CLS09 global mean dynamic topography computed from the combination of GRACE data, altimetry, and in situ measurements, *J. Geophys. Res.*, *116*, C07018, doi:10.1029/2010JC006505.
Roemmich, D., J. Gilson, R. Davis, P. Sutton, S. Wijffels, and S. Riser (2007), Decadal spinup of the South Pacific subtropical gyre, *J. Phys. Oceanogr.*, *37*, 162–173.
Rosell-Fieschi, M., S. R. Rintoul, J. Gourrion, and J. L. Pelegrí (2013), Tasman Leakage of intermediate waters as inferred from Argo floats, *Geophys. Res. Lett.*, *40*, 5456–5460, doi:10.1002/2013GL057797.
Samelson, R. M. (2011), *The Theory of Large-Scale Ocean Circulation*, 208 pp., Cambridge Univ. Press, New York.
Scully-Power, P. D. (1973), Coral Sea flow budgets in winter, *Aust. Mar. Freshwater Res.*, *24*(3), 203–216.
Speich, S., B. Blanke, P. De Vries, S. Drijfhout, K. Döös, A. Ganachaud, and R. Marsh (2002), Tasman leakage: A new route in the global ocean conveyor belt, *Geophys. Res. Lett.*, *29*(10), 1416, doi:10.1029/2001GL014586.
Stanton, B. R. (1979), The Tasman Front, *N. Z. J. Mar. Freshwater Res.*, *13*(2), 201–214.
Stanton, B. R., P. J. H. Sutton, and S. M. Chiswell (1997), The East Auckland Current, 1994–95, *N. Z. J. Mar. Freshwater Res.*, *31*(4), 537–549.
Sun, C., M. Feng, R. J. Matear, M. A. Chamberlain, P. Craig, K. R. Ridgway, and A. Schiller (2012), Marine downscaling of a future climate scenario for Australian boundary currents, *J. Clim.*, *25*(8), 2947–2962.
Suthers, I. M., et al. (2011), The strengthening East Australian Current, its eddies and biological effects—An introduction and overview, *Deep Sea Res., Part II*, *58*(5), 538–546.
Thompson, K. R., and E. Demirov (2006), Skewness of sea level variability of the world's oceans, *J. Geophys. Res.*, *111*, C05005, doi:10.1029/2004JC002839.
Tilburg, C. E., H. E. Hurlburt, J. J. O'Brien, and J. F. Shriver (2001), The dynamics of the East Australian Current system: The Tasman Front, the East Auckland Current, and the East Cape Current, *J. Phys. Oceanogr.*, *31*(10), 2917–2943.
Uppala, S. M., et al. (2005), The ERA-40 re-analysis, *Q. J. R. Meteorol. Soc.*, *131*(612), 2961–3012.
Wajsowicz, R. C. (1993), The circulation of the depth-integrated flow around an island with application to the Indonesian Throughflow, *J. Phys. Oceanogr.*, *23*(7), 1470–1484.
Wong, A. P. S., N. L. Bindoff, and J. A. Church (1999), Large-scale freshening of intermediate waters in the Pacific and Indian Oceans, *Nature*, *400*(6743), 440–443.
Wu, L., et al. (2012), Enhanced warming over the global subtropical western boundary currents, *Nat. Clim. Change*, *2*(3), 161–166.
Zlotnicki, V., L.-L. Fu, and W. Patzert (1989), Seasonal variability in global sea level observed with Geosat altimetry, *J. Geophys. Res.*, *94*(C12), 17,959–17,969.
Zwiers, F. W., and H. von Storch (1995), Taking serial correlation into account in tests of the mean, *J. Clim.*, *8*(2), 336–351.